Petroleum Science 23 (2026) 434–446

Contents lists available at ScienceDirect

Petroleum Science

journal homepage: www.keaipublishing.com/en/journals/petroleum-science

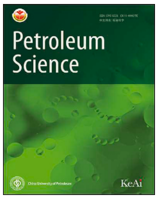

Original Paper

Unraveling the hydrodynamic effects on calcium carbonate scaling behavior under high-temperature and high-pressure CO_2 degassing

R.S. Maciel [a,*], F.A.R. Pereira [b], E.J. Soares [a], C. Scandian [a], J.R.C. Proveti [c], R.P. Cosmo [a], R.F. Fejoli [a], H.E.P. Schluter [d], A.L. Martins [d]

[a] *Department of Mechanical Engineering, Federal University of Espírito Santo, Vitória, ES, Brazil*
[b] *Department of Industrial Technology, Federal University of Espírito Santo, Vitória, ES, Brazil*
[c] *Department of Physics, Federal University of Espírito Santo, Vitória, ES, Brazil*
[d] *Petrobras, Rio de Janeiro, RJ, Brazil*

ARTICLE INFO

Article history:
Received 27 February 2025
Received in revised form
19 September 2025
Accepted 24 September 2025
Available online 30 September 2025

Edited by Yan-Hua Sun

Keywords:
Carbonate scaling
CO_2 degassing
Rotating cage
Hydrodynamic effect

ABSTRACT

Carbonate scaling in the Brazilian pre-salt oil production systems represents a challenging flow assurance issue driven by the release of CO_2 caused by head loss. This reduction in pressure causes CO_2 degassing, increases the pH and thereby promotes the $CaCO_3$ precipitation. Recent studies indicate that scaling rates intensify with the inherent flowing fluid turbulence. However, this phenomenon has not been comprehensively studied at elevated temperatures, pressures, and high CO_2 content, typical of pre-salt subsurface environments. This study uses a batch reactor equipped with a rotating cage system (according to the ASTM G184 standard) to investigate the effect of fluid dynamics on $CaCO_3$ scaling at up to 80 °C, 70 barg, different levels of turbulence and shear stress, being subjected to the effects of CO_2 degassing. Analyses were conducted using 3D profilometry, gravimetry, photomicroscopy, SEM, XRD, and Rockwell C scratch tests. The results reveal that, under oil well conditions, the turbulence distinctly influences the scaling rates compared to bench experiments (room temperature, atmospheric pressure, and without dissolved CO_2). What distinguishes the results of this study from other works is the appearance of a reversal point at sufficiently high turbulence—that is, the scaling rates begin to decrease with increased turbulence—still within the pre-salt oilwell operation range. The material adhered to the rotating cage coupons was investigated to understand this phenomenon, identifying that the calcium carbonate polymorphs contribute to this reversal.

1. Introduction

Inorganic carbonate scaling has become a significant operational challenge in oil production from Brazil's pre-salt reservoirs. Notably, calcium carbonate ($CaCO_3$) is the most common species in these assets (Bezerra et al., 2013). The reservoir rocks of the pre-salt are mainly carbonates and naturally supplies large amounts of ions, such as Ca^{2+} and HCO_3^-, which are the elements of the scaling problem. The fluids of these reservoirs also typically contain a high concentration of CO_2, with molar fractions reaching up to 79% in some cases (Souza et al., 2024). Pre-salt reservoirs generally experience pressures of around 500 bar or more (Fraga et al., 2015), and reservoir temperatures can reach 120 °C or higher (Gessner and Barbosa, 2022). Over geological time, these systems reach a thermodynamic equilibrium where high pressures cause CO_2 dissolution, keeping the chemical species in the aqueous solution, as expressed by Eq. (1):

$$Ca^{2+}\,(aq) + 2HCO_3^-\,(aq) \rightleftarrows CO_2\,(aq) + H_2O + CaCO_3\,(s). \tag{1}$$

The equilibrium partitioning of CO_2 between the aqueous and gaseous (or supercritical) phases is governed by the system's pressure and temperature conditions (Segev et al., 2012), as described by Eqs. (2) and (3). The more CO_2 dissolved in water, the greater the system's acidity, corresponding to a low pH value (Cosmo et al., 2019; Lower, 1999):

$$CO_2\,(aq) \rightleftarrows CO_2\,(g). \tag{2}$$

During oil production, the pressure drops, leading to CO_2 degassing, represented by a shift to the right side in the

---

* Corresponding author.
E-mail address: rodrigosimoesrsm@gmail.com (R.S. Maciel).
Peer review under the responsibility of China University of Petroleum (Beijing).

https://doi.org/10.1016/j.petsci.2025.09.040

equilibrium of Eq. (2) and characterized by an increase in the aqueous phase pH. This CO_2 exsolution triggers a perturbation in Eq. (1), shifting the equilibrium to the right side and driving the precipitation of $CaCO_3$. The precipitation process is further controlled by the solubility product of $CaCO_3$ (K_{sp}) and the acid-base equilibria of the carbonate system (Segev et al., 2012):

$$HCO_3^- \rightleftarrows H^+ + CO_3^{2-}, \tag{3}$$

where the carbonate ion (CO_3^{2-}) reacts with Ca^{2+} to form $CaCO_3$, according to the Eq. (4):

$$Ca^{2+} + CO_3^{2-} \rightleftarrows CaCO_3 \tag{4}$$

According to Frenier et al. (2008), the degassing of CO_2 from produced water is the key mechanism to explain the precipitation of calcium carbonate from a supersaturated water solution. As the pre-salt reservoirs have a high amount of dissolved CO_2, the $CaCO_3$ precipitation occurs in the earlier stages of oil production (Bezerra et al., 2013). This issue is expected to worsen as content increases with reservoir maturity (Cosmo et al., 2022).

The precipitation and scaling of calcium carbonate on production facilities such as valves, pipelines, and sand control screens reduce the available flow area, increasing pressure drop and reducing production capacity over time. In severe cases, this phenomenon can completely block flow. When it occurs in equipment like inflow control valves (ICVs), besides obstructing the valve narrow channels, it might cause the valve mechanisms to seize, sometimes requiring production shutdown and valve replacement in the production string, which is a costly operation.

Various factors contribute to inorganic scaling, including gas partial pressures (particularly CO_2), as explored by Cosmo et al. (2019) and Jamialahmadi and Müller-Steinhagen (2012), bulk temperature and water ionic concentration (Doubra et al., 2017; Dyer and Graham, 2002), flow conditions such as turbulence (Løge et al., 2022; Martins et al., 2020; Segev et al., 2012), and the presence of oil and gas phases (Cosmo et al., 2022). Properties of surface materials such as composition, roughness, wettability, and surface tension also play a significant role, as noted by Gong et al. (2024), Vazirian et al. (2016), Cheong et al. (2013), and Collins (2002). Moreover, scaling is linked to factors such as nucleation rates, crystal growth (Contreras et al., 2022; Dyer and Graham, 2002), polymorphism (Fathi et al., 2006), and the transport of chemical species or crystals to adhesion sites (Quan et al., 2008).

Recent studies have specifically emphasized the link between turbulence and scaling rates. Martins et al. (2020), Yan et al. (2017), Nichols et al. (2016), and Vazirian et al. (2016) have all contributed to understanding how turbulence impacts scaling. For example, Moriconi et al. (2021) demonstrated that calcium carbonate scaling initially increases with flow rate under turbulent conditions at pressures between 1 and 10 bar and ambient temperature (27 °C). After a certain turbulence level, the scaling plateaus, suggesting a shift in the deposition mechanism at higher flow rates. Similarly, Martins et al. (2020) explored calcium carbonate adhesion in a small-scale oil well completion valve under low pressure and ambient temperature conditions, finding that higher Reynolds numbers led to increased scaling rates, particularly near the valve's narrow channels, where wall shear stress and turbulence dissipation are relatively high, as discussed by Martins et al. (2020) and Graham et al. (2014).

Løge et al. (2022) used tomography imaging to assess the effects of turbulent flows and rough surfaces on barium sulfate ($BaSO_4$) scaling in an experimental valve. With the test solution maintained at 60 °C under low pressure, the results indicated that turbulence and rough surfaces led to increased scaling deposits. Vazirian et al. (2016) also investigated the effects of turbulence on scaling using a batch system with field water at 56 °C and environmental pressure. Their findings revealed that turbulence enhances scaling in both adhesion and deposition processes. Furthermore, the study showed that different surface coatings influence the extent of scaling, although turbulence generally amplifies scaling across various coatings.

According to Kadivar et al. (2021), in turbulent pipe flows, particles migrate toward walls via turbophoresis (turbulence-driven gradients), secondary flows induced by roughness, and near-wall sweep events. Roughness regimes modulate this transport: surface roughness enhances recirculation-driven deposition, while vortex shedding increases collisions. Turbulent fluctuations in the viscous sublayer further trap particles, with implications for scaling, as they augment both particle transport and retention near the wall. These mechanisms partially explain the observed hydrodynamic effects described by Løge et al. (2022) and Moriconi et al. (2021), whereby higher turbulence levels lead to increased scaling.

Zancanella et al. (2025) studied $CaCO_3$ scaling on 304 stainless steel under high CO_2 and flow conditions using a continuous flow apparatus, which included degassing part of the CO_2 through a local restriction valve at a constant flow rate and room temperature (resulting in the formation of only calcite crystals). They found that scaling increases with surface complexity (as measured by fractal dimension), not merely with roughness. High surface complexity may intensify interactions with the flowing fluid, modify the boundary layer, and generate a more turbulent and diffusive flow, thereby increasing the transport of crystal-forming species to the surface and enhancing adhesion.

The literature has not yet properly addressed the factors inherent in oil well environments, such as CO_2 degassing and high temperatures. It has been numerically (Cosmo et al., 2019) and thermodynamically (Cosmo et al., 2022) shown that CO_2 exsolution can contribute over 90% of the $CaCO_3$ precipitation. However, other effects of CO_2 degassing are not well established. Unlike temperature, which favors both $CaCO_3$ precipitation and the polymorphic change in crystals, as shown by Kawano et al. (2009). The authors observed that higher temperatures favor the stabilization of aragonite and vaterite alongside calcite.

Calcite, aragonite, and vaterite are the three non-hydrated polymorphic forms of calcium carbonate, each distinguished by its crystalline structure (Brečević and Kralj, 2007). Calcite, the most thermodynamically stable form, crystallizes in a trigonal rhombohedral structure. Aragonite forms in an orthorhombic crystal system with a needle-like shape (Lipus and Dobersek, 2007). Vaterite, the least stable polymorph, crystallizes in a hexagonal system and is often transient, commonly transforming into calcite or aragonite (Zhao et al., 2024).

Liendo et al. (2022) examines the synthesis of calcium carbonate ($CaCO_3$) via carbonation, emphasizing CO_2 sequestration and industrial waste utilization. The polymorph (calcite, aragonite, vaterite), morphology, and particle size depend on process conditions: pH (high pH favors calcite, low pH stabilizes vaterite), temperature (aragonite dominates > 40 °C, especially with Mg^{2+}), and supersaturation (high levels promote nanoparticle nucleation). Efficient CO_2 mass transfer, influenced by concentration, flow rate, and reactor design, is critical for achieving high carbonation rates.

According to Fathi et al. (2006), aragonite exhibits a very weak adhesion to the substrate, whereas calcite forms dense and tenacious layers, which are difficult to remove mechanically. Namely, while the temperature relates to the $CaCO_3$ scaling, the literature does not provide studies concluding a positive, neutral, or negative effect for an aqueous solution subjected to CO_2 partial pressure and degassing.

This study aims to investigate the impact of turbulence on $CaCO_3$ scaling under high-temperature and high-pressure CO_2 degassing conditions. Although there is evidence that suggests that elevated temperatures influence the underlying phenomena, the role of CO_2 degassing remains insufficiently explored. Thus, some tests were performed to illustrate the importance of including CO_2 degassing in the experimental matrix.

The basis of this study is experiments in a batch reactor equipped with a high-temperature and high-pressure pH probe. Turbulence was generated by a rotating cage attached to the reactor impeller, following the ASTM G184 standard (ASTM, 2016). Originally designed for corrosion evaluation (Xue et al., 2024), this setup has long been used to study inorganic scaling (Goodwin et al., 2018; Nichols et al., 2016; Graham et al., 2014; Silvestri et al., 2010). The rotating cage holds thin plates (coupons) that either lose mass due to corrosion, or gain mass due to particle deposition, when used in scaling experiments.

The experimental results were evaluated by measuring mass changes in coupons, testing adhesion friction resistance with Rockwell C scratch tests, and analyzing solid deposits using 3D profilometry, gravimetry, photomicroscopy, SEM, and XRD to correlate mass and adhesion force with calcium carbonate polymorphs.

2. Materials and methods

The experimental unit employed in this work was specially design to meet requirements for investigating flow assurance phenomena in the pre-salt context (Fig. 1(a)). Additional details can be found in Cosmo et al. (2023). Precipitation and scaling tests were carried out under high-temperature, high-pressure, and shear conditions, enabling control of $CaCO_3$ precipitation due to CO_2 degassing.

The batch reaction system controls reactants injection, rotational velocity, and temperature, with the solution pH monitored over time. It has a transparent side-viewing window for solution, reaction, and crystal growth visualization. The vessel and coupon-holding system, with adaptations, comply with the ASTM G184 standard (ASTM, 2016). The necessary adaptations and experimental steps were established based on a series of preliminary experiments and computation fluid dynamic simulations. These efforts allowed the definition of several key parameters, including the sequence of experimental steps, the configuration of double coupons in each rotating cage (RC) slot, the vertical positioning of the cage relative to the coupons' axis, and the mixing scheme for the reactive solutions under high-pressure and high-temperature conditions using a pressurized pipette.

Significant differences in hydrodynamic variables, such as velocity gradient and wall shear stress, can occur between the internal and external faces of coupons in rotating cage systems. This makes it difficult to directly correlate mass gain with these variables in scaling studies. To address this, a pair of half-thickness coupons were installed in each slot of the rotating cage (Fig. 1 (c)), allowing separate measurement and correlation of mass gain for each face under its respective hydrodynamic condition.

The average wall shear stress on the coupons was quantified according to the ASTM G170 standard (ASTM, 2006) and Vazirian et al. (2016). For RC rotational velocities of 0, 50, 125, 200, and 300 rpm, Eq. (5) estimates mean wall shear stresses (τ_w) at external coupons of 0, 0.1599, 0.9993, 2.5581, and 5.7558 Pa, respectively, for a 60 °C solution ($\rho = 984.98$ kg/m^3, $\mu = 5.59 \times 10^{-4}$ Pa·s (Kestin et al., 1978)).

$$\tau_w = 0.0791 Re^{-0.3} \rho R^2 \omega^{2.3} \tag{5}$$

where Re is the Reynolds number; ω is the angular velocity; R is the rotating cage radius; and ρ is the fluid density.

The coupons were prepared using a tumbling technique to ensure uniform surface roughness. This treatment not only standardizes the roughness across all coupons but also aligns their roughness magnitude with the surface finish of well completion valves. These valves are commonly identified as prone to fouling due to turbulence generation and significant localized pressure losses at the throat (Martins et al., 2020; Graham et al., 2014). To estimate roughness, 3D optical profilometer measurements were performed according to ISO 4287 standard (ISO, 1997) and Mirabal et al. (2023). As presented in Fig. 1(d), analysis of nine points across 30 coupons revealed a normal, random, and homogeneous roughness distribution.

The average roughness (R_a) was 0.324±0.095 μm in the horizontal direction and 0.569±0.149 μm in the axial direction. Fig. 2 shows that both linear and surface average roughness were statistically in the same magnitude order, allowing the assumption that roughness is similar between the coupons. Fig. 2 also shows the corresponding S_a values, a three-dimensional extension of R_a, used to describe the arithmetic mean of the absolute heights on a 3D surface.

The reaction medium is formed by mixing an anionic solution with a cationic solution and injecting pure gaseous carbon dioxide. Both solutions were prepared with distilled water, containing 37.48 mmol/L of sodium bicarbonate and 74.99 mmol/L of calcium chloride dihydrate, respectively.

The experiments were conducted at 60 and 80 °C, with the maximum temperature limited to 80 °C due to the pH probe's capacity. The pH, an important parameter when CO_2 is present, was monitored in real-time by the probe. The high-pressure CO_2 degassing is 50 barg and represents CO_2 partial pressure before the flash (before the CO_2 exsolution). In some runs, CO_2 partial pressure is the total pressure. In other tests, it was injected N_2 to reach 70 barg (total pressure), so the CO_2 partial pressure is 71%. It represents some pairs of pressures and CO_2 content in the gas phase. For example, 50 barg of pure CO_2 equals a total pressure of 250 barg with 20% of CO_2 content. The system can reach up to 110 barg; however, it was determined that a pressure of 50 barg of CO_2 is sufficient to represent the conditions of interest in this study.

To confirm that CO_2 degassing must be part of the experimental matrix, some preliminary assays were performed. The tests were conducted at 80 °C with a rotation of 200 rpm and injecting CO_2 to reach 50, 15, or 0 barg (no CO_2 injection, subjected to atmospheric air). The reactants (presented above) and the experimental procedure (to be detailed below) were similar to the main matrix. Some technique analyses were also applied to identify, quantify, and understand the scaling. In the two cases with CO_2, materials with different morphology were observed and more mass than in the case without CO_2. Furthermore, in the essays with CO_2, the material adhered (impregnated, scaled) to the coupons, while without CO_2, the material just deposited (settled, rested) to the coupons. It was sufficient to incorporate the CO_2 degassing effects in the experimental matrix. A more detailed discussion lies beyond the scope of this study, although Fig. 3 presents preliminary observations of adhered mass on the coupons under these conditions. The mass measurement was averaged across eight internal and external coupons, highlighting the significant role of CO_2 in adhesion. This opens a new field of study, requiring further research to deepen the understanding of carbonate scaling in CO_2-rich environments, such as Brazil's pre-salt reservoirs, where high CO_2 molar fractions are dissolved in water and oil phases.

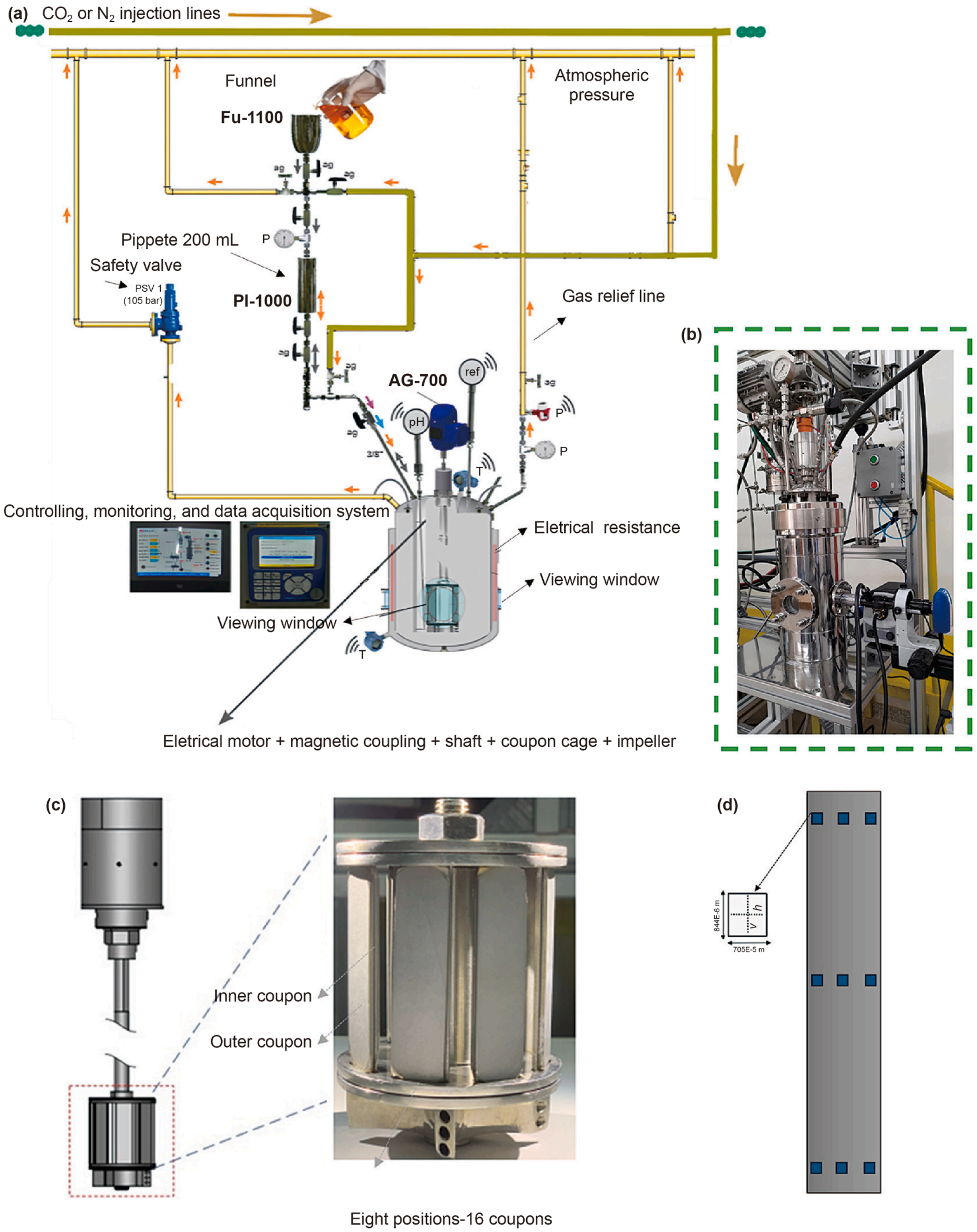

Fig. 1. (**a**) Schematic diagram of experimental setup with feeding and relief lines, an injection system, a reactor with rotating cage, and a controlling, monitoring, and data acquisition system. (**b**) Front view of the reactor. Left: coupon-holding cage attached to the axis. Right: split coupons (60.4 mm in length, 14 mm in width, 1.5 mm in thickness) in the rotating cage. (**c**) Rotating assembly with coupon cage. Coupon sampling point on the right. (**d**) Coupon analysis points for surface characterization.

In the main experiments, for each test, a 3 L solution was made with 2.9 L of $NaHCO_3$ solution and 0.1 L of $CaCl_2·2H_2O$ solution. At first, the anionic solution was pressurized with gaseous CO_2 at 50 barg for 1 h until pressure and pH stabilization, then heated to 60 or 80 °C. After heating, it was mixed with 0.1 L of cationic solution previously placed in a pipette (illustrated in Fig. 1(a)). This solution is injected into the reactor and mixed with the bicarbonate solution by pressurizing the pipette with 70 barg of N_2. After mixing, maintaining a rotational velocity of 125 rpm, and letting time for pH stabilization, a release valve was opened to allow degassing, triggering the precipitation reaction (Eqs. (1) and (2)). After the valve opening, different rotational velocities of 0, 50, 125, 200, and 300 rpm were used to simulate various flow conditions, with 300 rpm being the maximum for safety. To illustrate the experiments, Fig. 4 shows the precipitation process after degassing, highlighting gas bubbling and the increase in turbidity over time.

Fig. 5 shows pH values of the aqueous solution during different experimental stages for the 50, 125, and 200 rpm tests. Each stage—pressurizing with CO_2 (I), heating the solution (II to III), injecting $CaCl_2·2H_2O$ solution (IV), degassing the reactor (V), maintaining rotational velocity (V to VI), and opening the reactor (VI)—affects the chemical dynamics and pH response, influenced

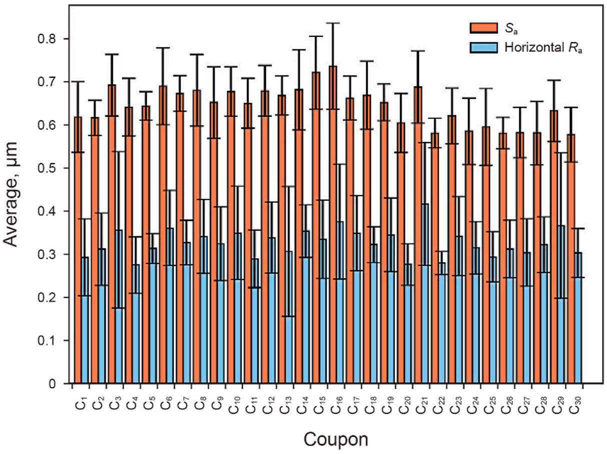

Fig. 2. Average roughness in the horizontal direction (measured along a line in two dimensions) and average S_a (the average surface roughness measured in three dimensions over the sample area) for coupons 1 to 30.

by temperature, pressure, and CO_2 levels. The degassing process reduces the CO_2 concentration and increases the solution's pH, leading to calcium carbonate precipitation, as indicated by the increased turbidity in Fig. 4.

After the tests, the coupons were dried in a glass desiccator for 24 h, and the scaling mass was measured according to the ASTM G184 standard (ASTM, 2016) by weighing each coupon (each half) before and after the test to account for the mass gain. The scaling mass was averaged between the eight internal and eight external coupons, and the scaling growth rate was calculated in millimeters per year (mm/year) by considering the test duration after degassing, the reference density of calcium carbonate (2790 kg/m^3—a weighted $CaCO_3$ polymorphs average density, representative of the assays in this study), and the average mass gain, using Eq. (6).

$$L = 0.845\overline{m} \tag{6}$$

where L is the scaling growth rate, mm/year; $\overline{m}$ is the average mass of the internal or external coupon, g; A is the flow exposed coupon area, mm^2; t is the test time after the degassing step, h; ρ_{CaCO_3} is the density of calcium carbonate, kg/m^3.

Scanning electron microscopy (SEM), optical microscopy, and optical 3D profilometry provide detailed insights into crystal morphology and surface distribution, while X-ray diffraction (XRD) elucidates the proportions of polymorphs present in the scaling samples. XRD, together with SEM, enables the identification and quantification of the proportions of different polymorphs adhered to the surfaces. The results of these analyses help establish a correlation between hydrodynamics and scaling phenomena under test conditions at 60 and 80 °C. These analyses are complementary to gravimetry and aim to reveal the role of temperature in polymorphism and the effect of hydrodynamics on scaling deposits from a microscopic perspective.

Subsequently to gravimetric analysis, sclerometry tests were performed on coupon surfaces to quantify the coefficient of friction (COF) under a linear ramp of normal load (0.5–10.5 N). This test (also called Rockwell C scratch test), conducted according to the ASTM C1624-05 standard (ASTM, 2005), assesses coatings' adhesion strength and failure mechanisms. This complements the gravimetric data, while microscopic evaluation helps uncover the hidden scaling mechanisms influenced by rotational velocity and temperature.

3. Results and discussion

This section presents the results obtained from the experimental procedures outlined, focusing on the scaling behavior of calcium carbonate under varying flow conditions and temperatures. The data collected from the batch reactor experiments, including scaling rates, crystal morphology, and the effects of CO_2 degassing, are analyzed in relation to the key variables of rotational velocity and temperature. The following analysis provides a detailed examination of the observed scaling phenomena.

Fig. 6 illustrates the accumulated scaling on the internal and external coupons at both temperatures. At 60 °C, the external coupons exhibited qualitatively more scaling than the internal ones, with deposit volumes increasing up to a specific rotational

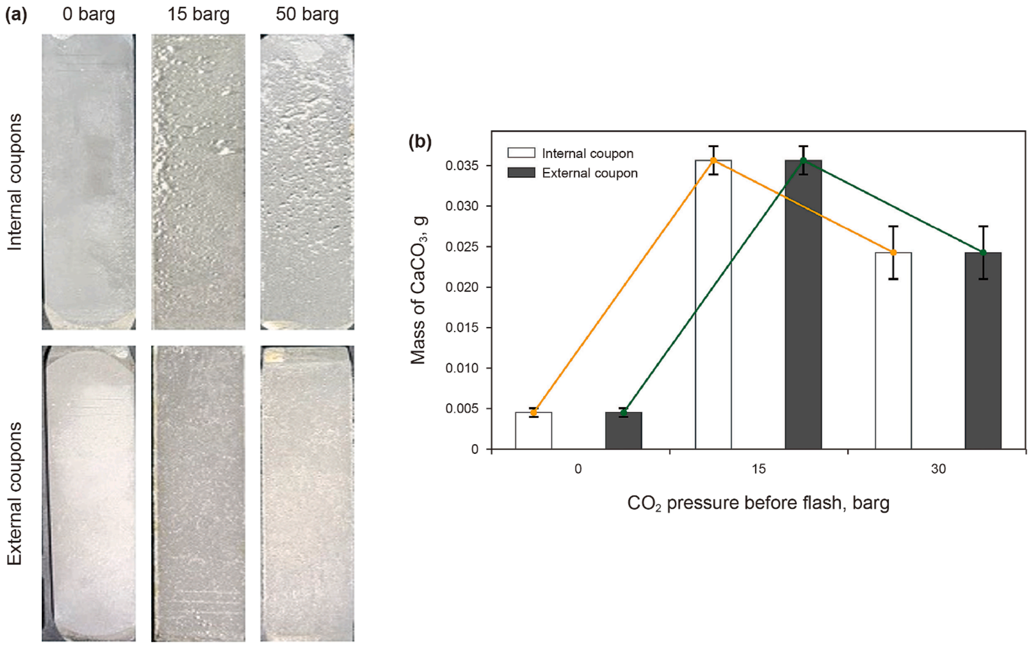

Fig. 3. Qualitative and quantitative scales aspect in the coupons in assays with CO_2 degassing (50 and 15 barg) and in the assay without CO_2 degassing (0 barg).

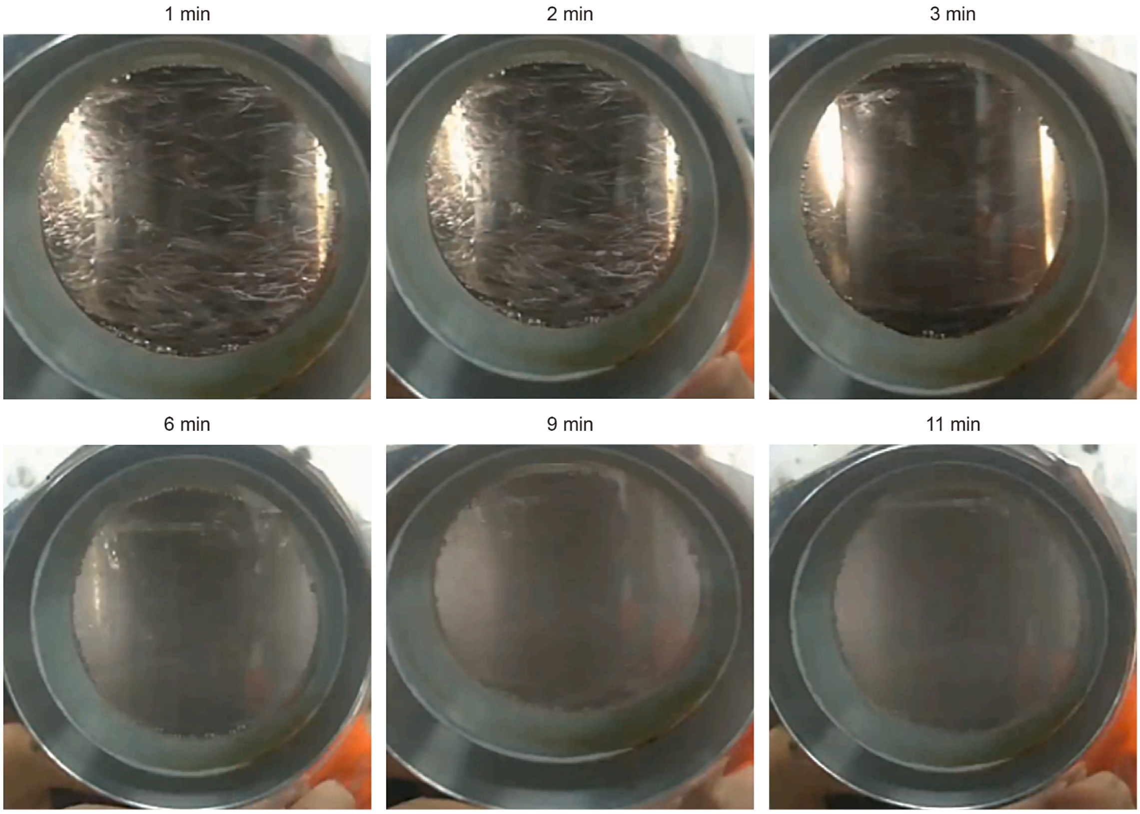
1 min 2 min 3 min

6 min 9 min 11 min

Fig. 4. Frontal viewing window images of the reactor at different moments after degassing.

threshold. Beyond this threshold, the scaling amount decreased as shear stress exceeded the adhesion forces, leading to crystal detachment from the surface.

At 80 °C, however, the distribution of calcium carbonate crystals remained consistent across different rotational velocities, suggesting a reduced influence of flow intensity at higher temperatures. This behavior indicates that at elevated temperatures, factors such as crystal stability and the relative proportions of calcium carbonate polymorphs, such as aragonite and calcite, may play a more dominant role than flow-induced effects alone.

Mass gain measurements and scaling rate estimates calculated using Eq. (6), provide average values and experimental deviations from eight internal and external coupons. This behavior, illustrated in Fig. 7, is particularly noticeable in the 60 °C tests. The high amplitude of some experimental deviation bars is associated with a significant presence of aragonite crystals on the coupon surfaces.

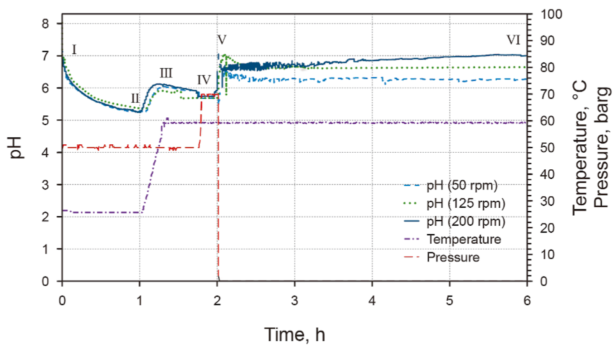

Fig. 5. pH dynamics across operational phases for the 50, 125, and 200 rpm tests.

This is evident because the deviations are reduced under conditions where aragonite crystals do not efficiently deposit over calcite crystals, as observed for certain temperature and shear conditions.

The overall trend indicates a dynamic balance between the transport and removal rates of material as rotational velocity increases. At 60 °C, scaling rates initially increased with velocity, peaking between 50 and 125 rpm, and then decreased while remaining higher than under static conditions. This suggests that increased shear is insufficient to completely remove the scaling, as the overall scaling rate continues to rise, albeit with a decreasing trend within the range of 125–300 rpm. At 80 °C, a similar inflection point was observed at higher velocities (200–300 rpm), likely due to the greater stability of aragonite crystals at elevated temperatures and the smaller average wall shear stress, as well as the lower average shear stress on the test coupon surfaces at 80 °C compared to 60 °C, as shown in Fig. 8. Despite the reduction in scaling rates at higher velocities, for both test temperatures, the rate at 300 rpm remains higher than under static conditions.

Aragonite crystals, although less stable than calcite under standard conditions (Kawano et al., 2009), exhibit greater stability at higher temperatures, such as 80 °C, compared to 60 °C. This promotes their preferential precipitation at elevated temperatures, even though calcite crystals are still observed in smaller quantities.

Higher temperatures accelerate crystal precipitation and growth rates while fostering agglomeration in the bulk phase (Zauner et al., 2000). Once formed, these agglomerates are more likely to be carried away by the flow due to fluid drag, reducing the amount of material that effectively adheres to the coupon. This drag-out effect leads to the lower adhered mass rate observed in

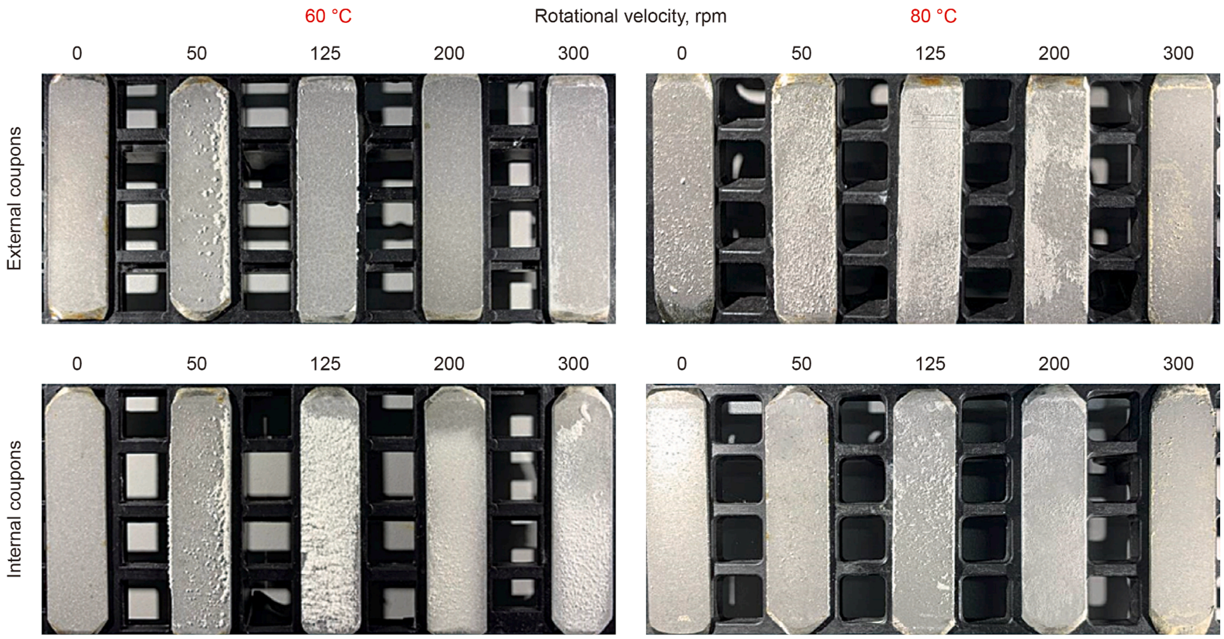

Fig. 6. Calcium carbonate deposits on the internal and external coupons for tests at 0, 50, 125, 200, and 300 rpm for 60 and 80 °C tests.

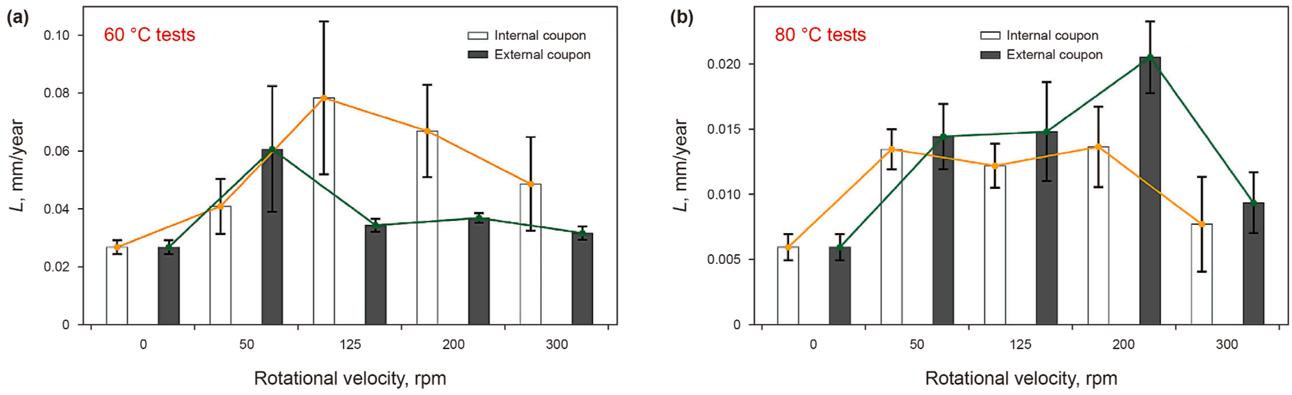

Fig. 7. Scaling rate dependency on flow intensity and rotational velocity.

tests conducted at 80 °C, despite similar wall shear stress compared to tests at 60 °C.

According to Quan et al. (2008), the stabilization of the scaling layer is due to a balance between deposition and removal rates. The deposition rate is influenced by two main effects: the transport of precipitated crystals or clusters from the bulk to the surface, driven by turbulent diffusion, turbophoresis, and inertial deposition, and the diffusion of chemical species (Ca^{2+} and CO_3^{2-}), leading to heterogeneous nucleation directly on surfaces.

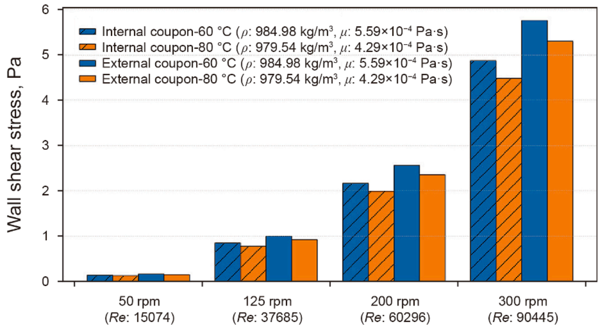

Fig. 8. Wall shear stress on internal and external coupon surfaces under different rotational conditions for 60 and 80 °C tests (internal diameter of 50.70 mm and external diameter of 57.15 mm).

The removal term, on the other hand, is associated with wall shear stress, which can reduce deposition by increasing fluid drag forces that exceed adhesion forces or by directly removing deposited material, depending on the stress intensity and the scale's resistance. Additionally, temperature plays a critical role, influencing polymorph stabilization, precipitation rates, and crystal growth, thereby indirectly affecting both transport and removal processes.

Fig. 8 shows the average shear stress on the internal and external surfaces of the coupons, estimated using Eq. (5), considering the properties of water, with density and viscosity varying with temperature as per Kestin et al. (1978). Shear stress estimates, based on the ASTM G170-06 standard (ASTM, 2006), indicate higher surface shear stress compared to internal surfaces, and show, more clearly for higher rotational velocities, that the shear stress is lower at the higher temperature.

Shear stress values are higher at 60 °C compared to 80 °C for the same rotational velocities on both internal and external coupons. This difference is attributed to the lower fluid viscosity at 80 °C, which reduces the resistance to flow. Consequently, the scaling rate turning point at 60 °C occurs at a lower rotational velocity.

At 80 °C, the reduced shear stress coincides with a higher proportion of aragonite relative to calcite, as evidenced by microscopic images (Figs. 9 and 10) and XRD compositional analysis (Fig. 11). The shift in polymorph proportion, whether precipitated in the fluid or directly on the wall, significantly impacts the transport of materials to surfaces and their removal, with fluid dynamics playing a key regulatory role.

Overall, the results at both test temperatures suggest a dynamic balance between scaling and removal rates (or the prevention of deposition), controlled by rotational velocity and wall shear stress. This finding contrasts with previous studies, which predominantly show that turbulence accelerates calcium carbonate scaling under low-temperature conditions near ambient environments (Moriconi et al., 2021; Martins et al., 2020; Vazirian et al., 2016), without presenting a turning point. At lower temperatures, calcite is the dominant calcium carbonate polymorph (Kawano et al., 2009), likely due to its higher mechanical strength and resistance to fluid shear compared to aragonite and vaterite. This increased resistance may dampen the effect of shear stress, reducing the impact of flow on calcite's detachment compared to the weaker aragonite crystals.

To enhance the phenomenological analysis of scaling and complement the assessment of scale mass, microscopic images were analyzed to uncover key aspects of adhesion and precipitation (Figs. 9 and 10). Additionally, compositional characteristics were examined through XRD analysis (Fig. 11), while the resistance of scaling to shear stress was investigated using scratch tests (Figs. 12–14). These analyses contribute to a deeper understanding of the scaling process and clarify several points, such as the relationship between temperature and polymorphism, as well as how different crystal types and proportions interact with fluid flow.

SEM images from the 60 °C scaling test on the external coupon surfaces revealed four distinct calcium carbonate crystal types: rhombohedral calcite, acicular or hexagonal aragonite, and flower-like vaterite (Figs. 9 and 10). At 0 rpm, the surfaces were predominantly covered with calcite crystals. At 125 rpm, a stable mixture of vaterite and aragonite appeared alongside calcite, likely due to enhanced transport of calcium carbonate crystals or ions to the surface. At 300 rpm, the proportion of vaterite and aragonite decreased, leaving calcite as the dominant crystal type, similar to the 0 rpm condition but with a slightly higher scaling rate. Additionally, SEM images showed that crystals formed at 0 rpm were larger than those at 300 rpm, indicating that higher rotational velocities inhibit crystal growth.

Fig. 9 also highlights the emergence of aragonite crystals from calcite interstices on the 0 rpm coupon substrate. These high-aspect-ratio aragonite crystals exhibit fragility due to their smaller cross-sectional area and reduced support from neighboring crystals, making them more susceptible to detachment under fluid shear or particle impacts in higher-flow conditions.

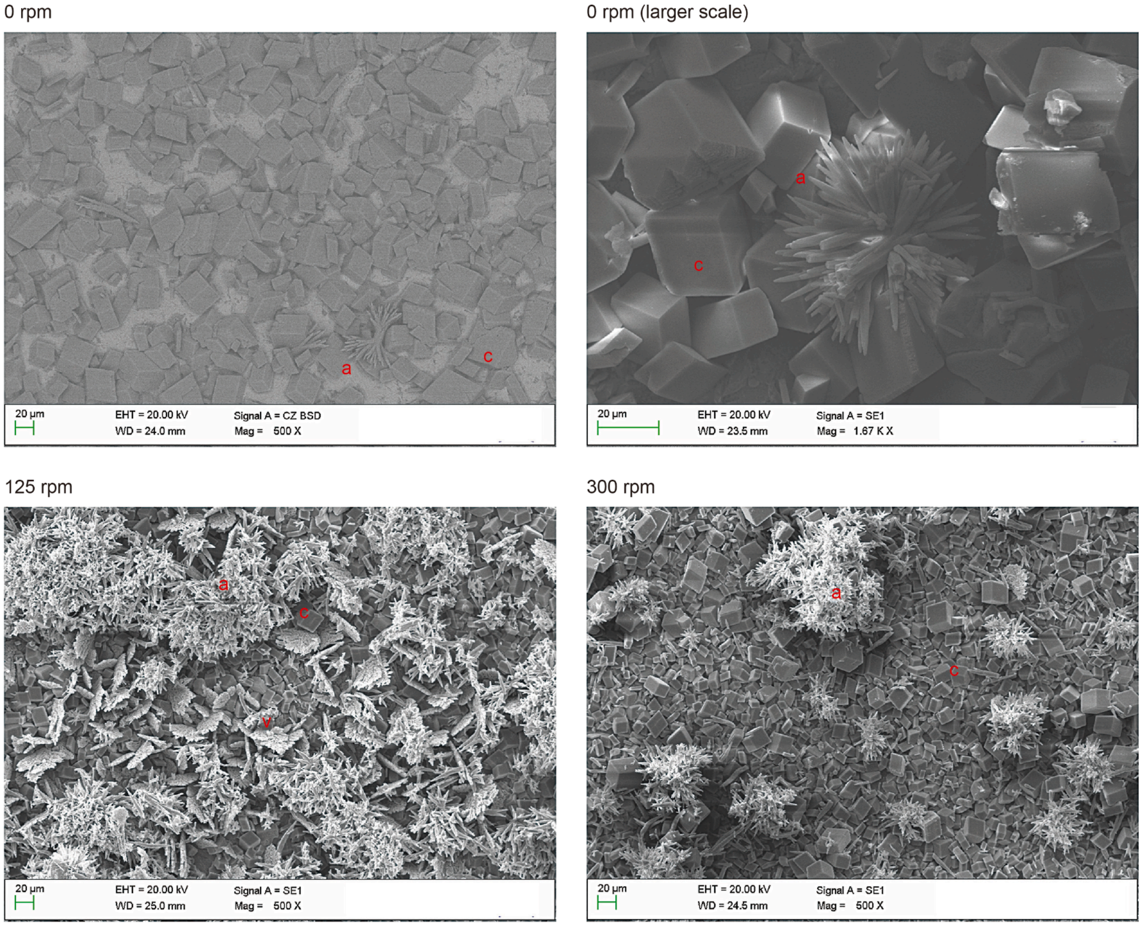

Fig. 9. SEM images illustrating calcium carbonate polymorphs under different rotational conditions, highlighting the polymorphs: calcite (c), vaterite (v), and aragonite (a), on the external surfaces, for 50 barg of CO_2 initial pressure at 60 °C tests.

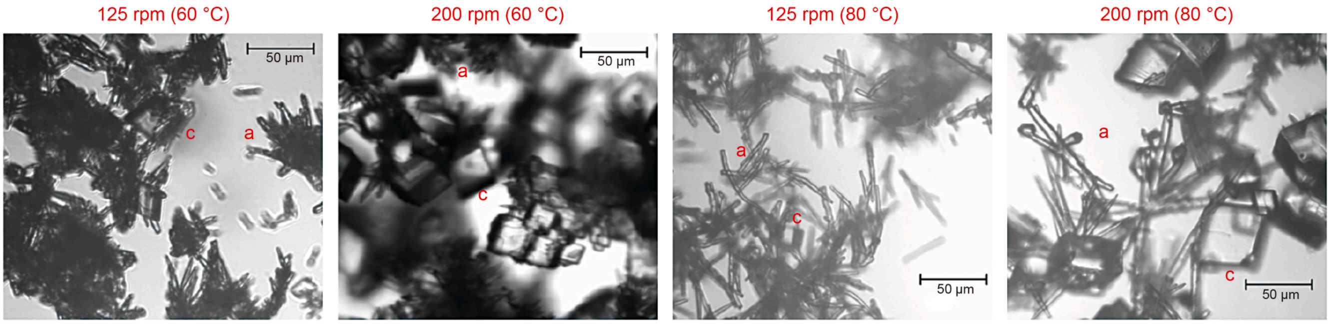

Fig. 10. Optical microscopy images of calcium carbonate polymorphs (calcite (c) and aragonite (a)) from bulk samples tested at 125 and 200 rpm, at bulk solution temperatures of 60 and 80 °C.

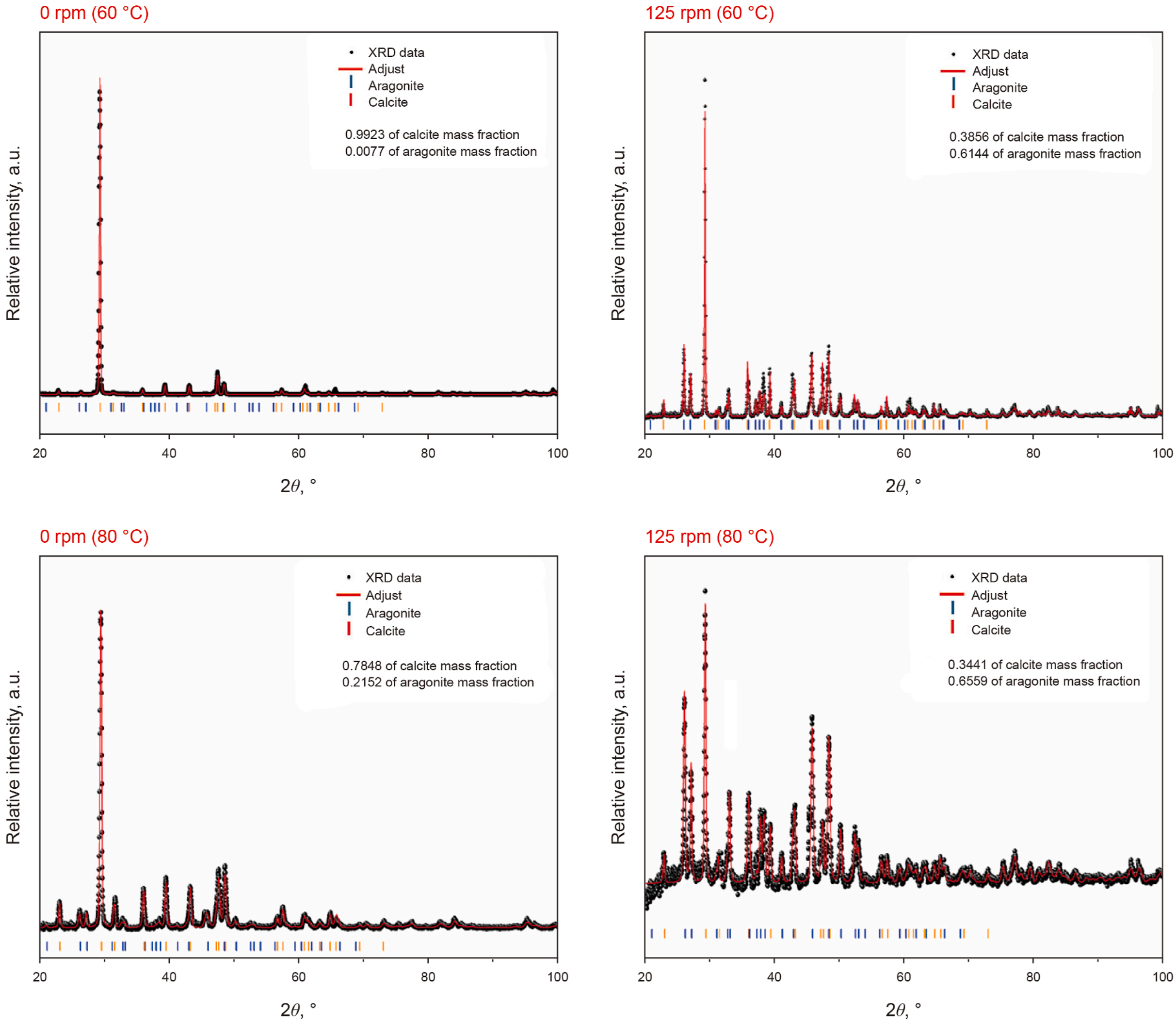

Fig. 11. XRD patterns.

The reduction in scaling rates at high turbulence levels (Fig. 7) requires careful interpretation. Although the overall deposition rate decreases, SEM images show a densely packed surface of calcite crystals at 300 rpm, with minimal voids between them—contrasting with the less compact distribution observed at 0 rpm under 60 °C conditions. Calcite's high shear resistance allows it to remain adhered even under intense flow conditions. While a lower deposition rate was observed at 300 rpm, the rate remained positive. Over an extended period, scaling would likely consist primarily of calcite, forming a tougher, more resilient deposit that could pose significant challenges for mitigation.

Optical microscopy of bulk samples collected after reactor opening for the 125 and 200 rpm tests at 60 and 80 °C (Fig. 10) revealed that higher temperatures lead to the formation of larger aragonite crystals. These larger particles or clusters are more effectively carried by turbulent flows due to their increased

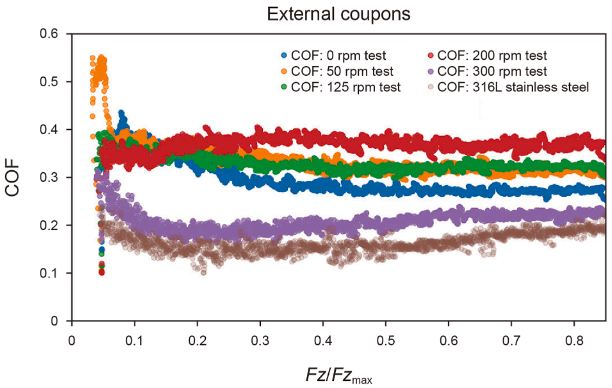

Fig. 12. Scratch friction coefficient (COF) in the normal load ramp normalized by the maximum vertical load, Fz_{max} (Fz is the vertical load applied by the indenter on the coupon surface along the linear scratch length, N), for internal and external coupons in the 60 °C tests conducted at rotational velocities of 0, 50, 125, 200, and 300 rpm.

surface area and lower density, as observed in the images. As more material remains suspended in the fluid, less material is available for deposition and adhesion. Additionally, aragonite crystals are more susceptible to shear forces due to their needle-like shape and smaller cross-sectional area, which contributes to the reduction in scaling rate at 80 °C. These images also show that as the rotational velocity increases, aragonite aggregates decrease in size, while calcite crystals grow, as also observed in Fig. 9 for the 60 °C tests.

XRD analysis of $CaCO_3$ samples from external coupons at both test temperatures reveals a mixed-phase composition of majority of calcite and aragonite. Fig. 11 illustrates that sharper peaks characterize calcites, while aragonite displays broader, less intense peaks.

These measurements corroborate that the turbulence effect, at both test temperatures, increases the mass fraction of aragonite at the expense of calcite. The higher relative intensity and distribution of aragonite peaks observed in samples from the 80 °C tests highlight the increased mass fraction of aragonite relative to calcite as the temperature rises. These findings are consistent with the microscopic observations presented in Figs. 9 and 10, confirming the dominant presence of these polymorphs and their indirect relationship with temperature and rotational velocity. These results align with those of Benkhaled et al. (2024), who analyzed calcium scaling from electrical submersible pumps (ESPs) in a carbonate reservoir with a low water cut (~1%). The scale was composed of 95% aragonite, which the authors attributed primarily to thermodynamic factors—particularly the high temperature that favors aragonite formation—as well as to hydrodynamic fluctuations and the turbulent flow regime within the ESP.

In addition to gravimetric measurements, microscopic analysis, and compositional analysis, Rockwell C scratch tests were performed on coupon surfaces. Fig. 12 shows the average COF over the normalized load ramp along the 10 mm scratch on external coupon surfaces at different rotational velocities. COF data from the 60 °C test and measurements on non-scaling 316L stainless steel coupons are scattered. Values are averaged from three scratches per coupon, with two coupons per velocity. Tests at 60 °C indicate that rotational velocity influences the COF, following a trend similar to the scaling rate: it increases with rotational velocity up to a peak, then decreases.

Higher COF values for coupons with scaling indicate increased resistance to the indenter's motion. Lower COF values for non-scaled coupons suggest easier sliding, likely due to higher surface hardness and lower roughness compared to scaled surfaces. This parameter indirectly correlates with the scaling layer's resistance,

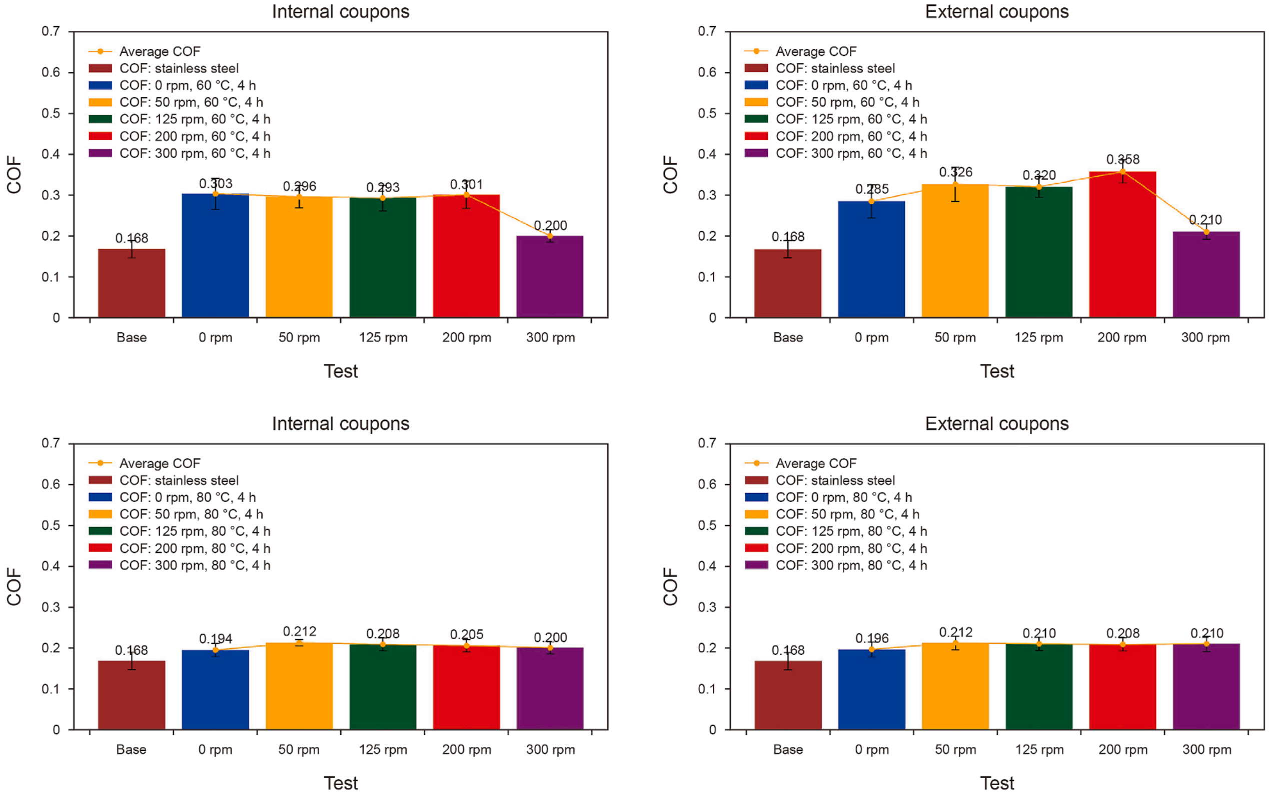

Fig. 13. Slide friction coefficient (COF) in the normal load ramp normalized by the maximum load for internal and external coupons in the 60 °C (above) and 80 °C (below) tests conducted at rotational velocities of 0, 50, 125, 200, and 300 rpm.

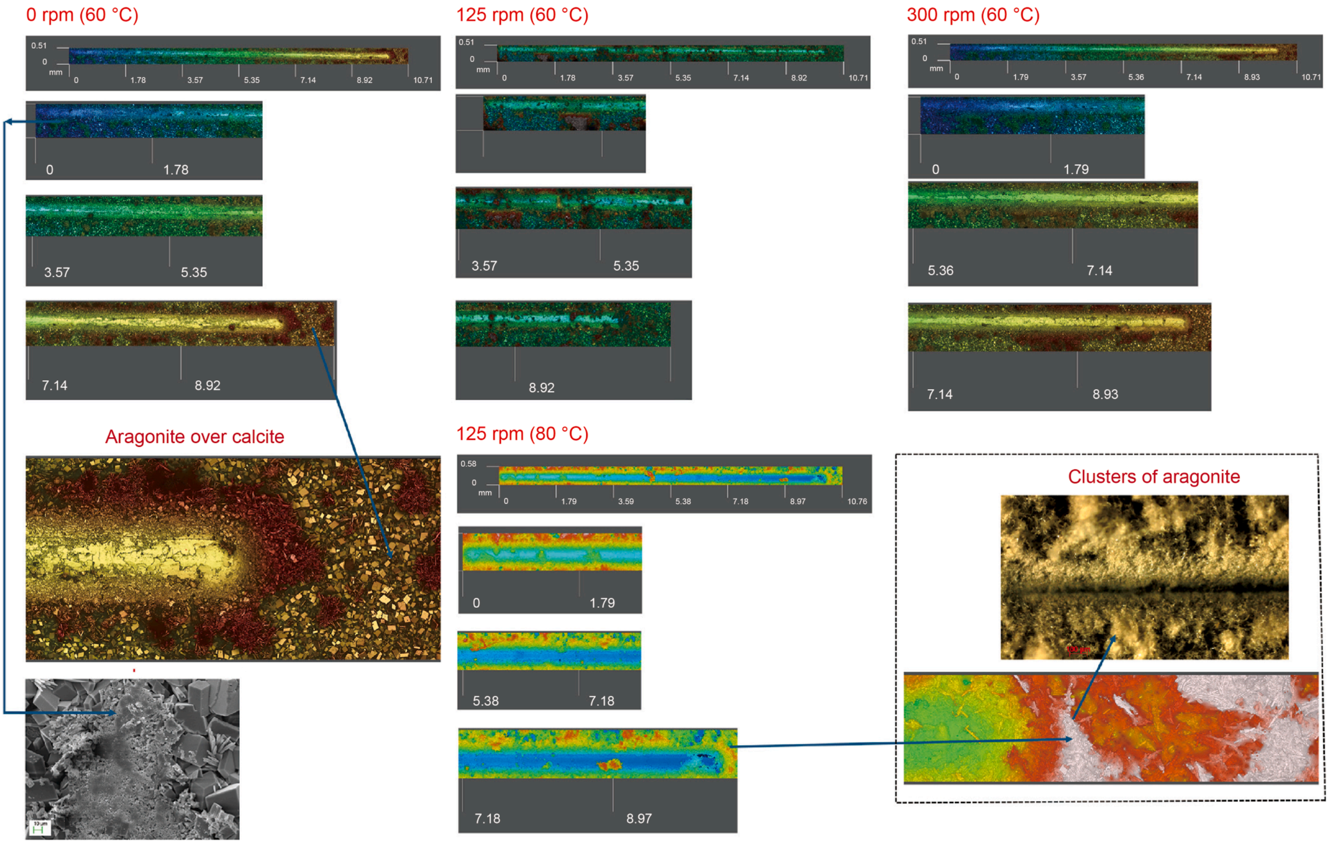

Fig. 14. Microscopic images from optical profilometry, SEM, and optical microscopy of scratches on external coupons at rotational velocities of 0, 125, and 300 rpm (60 °C) and 125 rpm (80 °C).

as the COF is the ratio of the frictional sliding force to the normal force.

Quantifying the average COF over scratches at different rotational velocities and temperatures (Fig. 13) shows that COF is less affected by rotational velocity at 80 °C compared to 60 °C. The average COF at 60 °C is higher than at 80 °C, and at 300 rpm, COF values exceed those of non-scaled coupons, indicating that high shear forces cannot completely prevent scaling. The results suggest that the indenter was unable to fully detach the scaling layer under all conditions, leaving material between the indenter and the stainless-steel surface. This is confirmed through linear optical profilometry images of the scratches (Fig. 14), which show the absence of collapse in the average COF over that measured on the stainless-steel coupon without scaling. In all cases, a compressed film of material is observed between the indenter and the metal tip. The scratch images also show a considerable accumulation of aragonite crystals on the coupon surface at 80 °C, although gravimetric measurements indicate a smaller mass compared to the results from the 60 °C tests. The lower COF value measured for the 80 °C coupons, along with the predominant aragonite coverage, suggests that this configuration is less resistant to the indenter's mechanical sliding within the linear ramp from 0.2 to 10.2 N.

Although derived from a batch reactor, these findings are significant, highlighting scaling behavior under various flow conditions and temperatures, and leading to distinct observations compared to studies that analyzed scaling at lower temperatures and in environments without CO_2 (Løge et al., 2022; Moriconi et al., 2021; Martins et al., 2020; Vazirian et al., 2016). These studies, which examined the effects of hydrodynamics on scaling behavior, have consistently shown that scaling rates tend to increase with turbulence intensity. These differences underscore the importance of considering variable temperatures in experimental analyses of calcium carbonate scaling.

The CO_2 degassing effect, which initiates the precipitation reaction, was also an important variable, resulting in an increased deposition mass compared to non-CO_2 conditions. The degassing effect creates a chemical potential that drives the system toward a new equilibrium state, thereby accelerating the precipitation rate and increasing scaling mass. This study is a pioneering effort in considering this effect with a high degree of control.

4. Conclusions

Through a systematic application of the developed methodology, this study unveils the intricate relationship between hydrodynamics, temperature, and CO_2 content in calcium carbonate scaling under high-temperature and high-pressure wellbore conditions. Gravimetric analysis quantified scaling rates at 60 and 80 °C, both at 70 barg, while X-ray diffraction (XRD) identified and measured polymorph distributions influenced by temperature. Scanning electron microscopy (SEM) and optical microscopy provided detailed insights into crystal morphology and surface adhesion patterns. Additionally, scratch tests evaluated the mechanical resistance of scaling to shear forces. Collectively, these techniques have enhanced the understanding of the scaling process and adhesion strength, emphasizing the role of hydrodynamics and its effects at elevated temperatures. Hydrodynamics directly impacts scaling through a dual mechanism: It enhances the mass transfer of bulk particles or chemical species to the adhesion surface, but, when shear forces exceed a critical threshold, mechanically removes the scale or inhibits its growth—particularly for less-adherent and less-resistant polymorphs.

The findings challenge the conventional assumption that turbulence intensity consistently promotes scaling. In contrast, our results indicate that while higher flow velocities initially increase scaling rates, beyond a certain threshold, turbulence inhibits adhesion due to elevated shear forces. This effect is particularly pronounced at 60 °C, where rotational velocity significantly influences scaling rates.

Temperature plays a crucial role in both precipitation rate and crystal polymorphism. As expected, tests conducted at 80 °C revealed a greater tendency for aragonite formation, which resulted in lower adhesion rates due to its less compact crystal structure. Conversely, at 60 °C, calcite predominates under higher shear conditions, potentially leading to long-term scaling challenges due to its greater resistance to detachment. The study's methodology, designed to replicate Brazilian pre-salt well conditions with a high CO_2 molar fraction and elevated temperatures, provides a valuable framework for further investigations in more complex and realistic environments, such as high-salinity solutions, mixed gas phases, and the presence of potential scaling inhibitors.

These insights contribute to a more refined understanding of scaling mechanisms in CO_2-rich systems, where temperature and hydrodynamic forces jointly influence scaling behavior.

Lastly, the batch rotating cage system, although it does not fully replicate the hydrodynamic characteristics of pipe flow due to inherent geometric discrepancies, provides substantial experimental advantages for scaling studies. Despite its relative simplicity, this system enables precise control and monitoring under high pressure and temperature conditions—parameters that are not commonly reported in the literature—while also facilitating the achievement of turbulent flow regimes. Scaling phenomena observed on test coupons can be quantitatively correlated with those observed in pipe flow through the application of equivalent wall shear stress matching (ASTM, 2016). Therefore, the results obtained may be further validated by comparative analysis with wellbore flow conditions, utilizing advanced computational fluid dynamics (CFD) methods.

CRediT authorship contribution statement

R.S. Maciel: Writing – review & editing, Writing – original draft, Validation, Data curation, Conceptualization. **F.A.R. Pereira:** Supervision, Project administration, Formal analysis. **E.J. Soares:** Writing – review & editing, Supervision, Formal analysis. **C. Scandian:** Methodology, Conceptualization. **J.R.C. Proveti:** Methodology, Conceptualization. **R.P. Cosmo:** Writing – review & editing. **R.F. Fejoli:** Visualization, Methodology. **H.E.P. Schluter:** Supervision, Resources, Methodology. **A.L. Martins:** Supervision, Methodology.

Declaration of competing interest

The authors declare that they have no known competing financial interests or personal relationships that could have appeared to influence the work reported in this paper.

Acknowledgments

This research was partially funded by grants from Petrobras, and CNPq (Brazilian Research Foundation).

References

ASTM, 2005. Standard Test Method for Adhesion Strength and Mechanical Failure Modes of Ceramic Coatings by Quantitative Single Point Scratch Testing (ASTM C1624-05). ASTM International.

ASTM, 2006. Standard Guide for Evaluating and Qualifying Oilfield and Refinery Corrosion Inhibitors in the Laboratory (ASTM G170-06). ASTM International.

ASTM, 2016. Standard Practice for Evaluating and Qualifying Oil Field and Refinery Corrosion Inhibitors Using Rotating Cage (ASTM G184-06). ASTM International.

Benkhaled, M., Tort, F., Baraka-Lokmane, S., Fretard, D., Lesage, N., 2024. Strategic scale mitigation for oil wells with a low basic sediment and water. In: SPE International Oilfield Scale Conference and Exhibition. https://doi.org/10.2118/218702-MS.

Bezerra, M.C.M., Rosário, F.F., Rosa, K.R.S.A., 2013. Scale management in deep and ultradeep water fields. In: Offshore Technology Conference. https://doi.org/10.4043/24508-MS.

Brečević, L., Kralj, D., 2007. On calcium carbonates: From fundamental research to application. Croat. Chem. Acta 80 (3–4), 467–484. https://doi.org/10.1002/chin.200805226.

Cheong, W.C., Gaskell, P.H., Neville, A., 2013. Substrate effect on surface adhesion/crystallization of calcium carbonate. J. Cryst. Growth 363, 7–21. https://doi.org/10.1016/j.jcrysgro.2012.09.025.

Contreras, V., Paz, P., Netto, T.A., 2022. Experimental analysis of inorganic scale deposition in pipes: Mesoscale flow loop development and case study. J. Petrol. Sci. Eng. 209, 109776. https://doi.org/10.1016/j.petrol.2021.109776.

Collins, I.R.. 2002. A new model for mineral scale adhesion. In: SPE International Oilfield Scale Conference and Exhibition. https://doi.org/10.2118/74655-MS.

Cosmo, R.P., Pereira, F.A.R., Ribeiro, D.C., Barros, W.Q., Martins, A.L., 2019. Estimating CO_2 degassing effect on $CaCO_3$ precipitation under oil well conditions. J. Petrol. Sci. Eng. 181, 106207. https://doi.org/10.1016/j.petrol.2019.106207.

Cosmo, R.P., Pereira, F.A.R., Soares, E.J., Martins, A.L., 2022. Modeling and validation of the CO_2 degassing effect on $CaCO_3$ precipitation using oilfield data. Fuel 310, 122067. https://doi.org/10.1016/j.fuel.2021.122067.

Cosmo, R.P., Rinaldi, R., Pereira, F.A.R., Soares, E.J., Martins, A.L., 2023. CO_2 degassing in $CaCO_3$ precipitation in the presence of oil: Implications, modeling, numerical simulation, validation, prototype development, and experimental results. Geoen. Sci. Eng. 228, 211885. https://doi.org/10.1016/j.geoen.2023.211885.

Doubra, P., Kamran-Pirzaman, A., Mohammadi, A.H., Hassanalizadeh, R., 2017. Thermodynamic modeling of scale (calcite, barite, anhydrite, and gypsum) deposition from brine. J. Mol. Liq. 230, 96–103. https://doi.org/10.1016/j.molliq.2016.11.135.

Dyer, S.J., Graham, G.M., 2002. The effect of temperature and pressure on oilfield scale formation. J. Petrol. Sci. Eng. 35 (1–2), 95–107. https://doi.org/10.1016/S0920-4105(02)00217-6.

Fathi, A., Mohamed, T., Claude, G., Maurin, G., Mohamed, B.A., 2006. Effect of a magnetic water treatment on homogeneous and heterogeneous precipitation of calcium carbonate. Water Res. 40 (10), 1941–1950. https://doi.org/10.1016/j.watres.2006.03.013.

Fraga, C.T., Capeleiro Pinto, A.C., Branco, C.C.M., de Sant́Anna Pizarro, J.O., da Silva Paulo, C.A., 2015. Brazilian pre-salt: An impressive journey from plans and challenges to concrete results. In: Offshore Technology Conference. https://doi.org/10.4043/25710-MS.

Frenier, W.W., Ziauddin, M., Wolf, N., Hartman, R., 2008. Formation, Removal, and Inhibition of Inorganic Scale in the Oilfield Environment. Society of Petroleum Engineers. https://doi.org/10.2118/9781555631406.

Gessner, T.R., Barbosa Jr, J.R., 2022. An internally consistent procedure to characterize single carbon number fractions for phase equilibrium of petroleum mixtures: Application to Brazilian pre-salt reservoir fluids. J. Petrol. Sci. Eng. 208, 109723. https://doi.org/10.1016/j.petrol.2021.109723.

Gong, L., Wu, F.Y., Pan, M.F., Huang, J., Zhang, H., Luo, J.L., Zeng, H.B., 2024. Exploring the mechanisms of calcium carbonate deposition on various substrates with implications for effective anti-scaling material selection. Pet. Sci. 21 (4), 2870–2880. https://doi.org/10.1016/j.petsci.2024.02.004.

Goodwin, N., May, M., Nichols, D., Graham, G., 2018. Scale deposition and hydrodynamics-benchtop to pilot rig. In: SPE International Oilfield Scale Conference and Exhibition. https://doi.org/10.2118/190756-MS.

Graham, G.M., Goodwin, N., Albino, E., Guan, H., Pinto, H.L., Bezerra, M., 2014. Minimizing scale deposition through surface enhancement in downhole tools. In: SPE International Oilfield Scale Conference and Exhibition. https://doi.org/10.2118/169781-MS.

ISO, 1997. Geometrical Product Specifications (GPS)—Surface Texture: Profile Method—Terms, Definitions and Surface Texture Parameters (ISO 4287:1997). International Organization for Standardization.

Jamialahmadi, M., Müller-Steinhagen, H., 2012. Crystallization Fouling. Encyclopedia of Desalination and Water Resources. www.desware.net.

Kadivar, M., Tormey, D., McGranaghan, G., 2021. A review on turbulent flow over rough surfaces: Fundamentals and theories. Int. J. Thermofluids 10, 100077. https://doi.org/10.1016/j.ijft.2021.100077.

Kawano, J., Shimobayashi, N., Miyake, A., Kitamura, M., 2009. Precipitation diagram of calcium carbonate polymorphs: Its construction and significance. J. Phys. Condens. Matter 21 (42), 425102. https://doi.org/10.1088/0953-8984/21/42/425102.

Kestin, J., Sokolov, M., Wakeham, W.A., 1978. Viscosity of liquid water in the range −8 °C to 150 °C. J. Phys. Chem. Ref. Data 7 (3), 941–948. https://doi.org/10.1063/1.555581.

Liendo, F., Arduino, M., Deorsola, F.A., Bensaid, S., 2022. Factors controlling and influencing polymorphism, morphology and size of calcium carbonate synthesized through the carbonation route: A review. Powder Technol. 398, 117050. https://doi.org/10.1016/j.ijft.2021.100077.

Lipus, L.C., Dobersek, D.J.C.E.S., 2007. Influence of magnetic field on the aragonite precipitation. Chem. Eng. Sci. 62 (7), 2089–2095. https://doi.org/10.1016/j.ces.2006.12.051.

Løge, I.A., Bentzon, J.R., Klingaa, C.G., Walther, J.H., Anabaraonye, B.U., Fosbøl, P.L., 2022. Scale attachment and detachment: The role of hydrodynamics and surface morphology. Chem. Eng. J. 430, 132583. https://doi.org/10.1016/j.cej.2021.132583.

Lower, S.K., 1999. Carbonate Equilibria in Natural Waters, vol. 544. Simon Fraser University, pp. 1–26. http://www.chem1.com/acad//webtext/pdf/c3carb.pdf.

Martins, A.L., Santos, H.F., Castro, B.B., Gonçalves, A.S., Maffra, D.A., Loureiro, J.B., 2020. Large scale laboratory tests for calcium carbonate scaling in sliding sleeve valves. In: SPE International Oilfield Scale Conference and Exhibition. https://doi.org/10.2118/200714-MS.

Mirabal, A., Loza-Hernandez, I., Clark, C., Hooks, D.E., McBride, M., Stull, J.A., 2023. Roughness measurements across topographically varied additively manufactured metal surfaces. Addit. Manuf. 69, 103540. https://doi.org/10.1016/j.addma.2023.103540.

Moriconi, L., Nascimento, T., de Souza, B.G.B., Loureiro, J.B.R., 2021. Top-down model of limescale formation in turbulent pipe flows. https://doi.org/10.48550/arXiv.2107.11463.

Nichols, D.A., Frigo, D.M., Graham, G.M., 2016. Advances in understanding effects of shear and turbulence on scale formation, adhesion and growth on surfaces. In: SPE International Oilfield Scale Conference and Exhibition. https://doi.org/10.2118/179903-MS.

Quan, Z., Chen, Y., Ma, C., 2008. Heat mass transfer model of fouling process of calcium carbonate on heat transfer surface. Sci. China E 51 (7), 882–889. https://doi.org/10.1007/s11431-008-0051-7.

Segev, R., Hasson, D., Semiat, R., 2012. Rigorous modeling of the kinetics of calcium carbonate deposit formation. AIChE J. 58 (4), 1222–1229. https://doi.org/10.1002/aic.12645.

Silvestri, M.A., Emmons, D.H., Linares-samaniego, S., Gingrich, R., 2010. Development of a combination corrosion-scale inhibitor for the subsea separation and boosting systems of the Parque das Conchas project in Brazil. In: Offshore Technology Conference. https://doi.org/10.4043/20371-MS.

Souza, A.C., da Silva Calixto, E.E., Pessoa, F.L.P., da Silva, V.L., Pereira, L.O.V., 2024. Modelling a CO_2 meter for a petroleum multiphase mixture at subsea conditions. Flow Meas. Instrum. 95, 102489. https://doi.org/10.1016/j.flowmeasinst.2023.102489.

Vazirian, M.M., Charpentier, T.V., de Oliveira Penna, M., Neville, A., 2016. Surface inorganic scale formation in oil and gas industry: As adhesion and deposition processes. J. Petrol. Sci. Eng. 137, 22–32. https://doi.org/10.1016/j.petrol.2015.11.005.

Xue, H., Gao, Q., Zhao, Y., Li, X., Chen, J., Zhang, T., Wang, F., 2024. A life prediction model for P110S steel in deep-well environments with H_2S/CO_2 coexistence based on multi-factor chemometric drive. Corros. Sci. 112475. https://doi.org/10.1016/j.corsci.2024.112475.

Yan, F., Zhang, F., Bhandari, N., Ruan, G., Alsaiari, H., Dai, Z., Tomson, M., 2017. The effect of turbulence on mineral scale control in oilfield. In: SPE International Conference on Oilfield Chemistry. https://doi.org/10.2118/184524-MS.

Zancanella, A.C.B., Saidler, L.A., Siqueira, R.D.N., Schluter, H.E.P., Loureiro, B.V., 2025. Evaluation of the surface finish on 304 stainless steel as a way to mitigate calcium carbonate scaling. Surfaces 8 (1), 13. https://doi.org/10.3390/surfaces8010013.

Zauner, R., Jones, A.G., 2000. Mixing effects on product particle characteristics from semi-batch crystal precipitation. Chem. Eng. Res. Des. 78 (6), 894–902. https://doi.org/10.1205/026387600527969.

Zhao, D., Williams, J.M., Hou, P., Moment, A.J., Kawashima, S., 2024. Stabilizing mechanisms of metastable vaterite in cement systems. Cem. Concr. Res. 178, 107441. https://doi.org/10.1016/j.cemconres.2024.107441.